# RD39 STATUS REPORT

# RD39 Collaboration

K. Borer, S. Janos and K. Pretzl
*Laboratorium für Hochenergiephysik der Universität Bern, Sidlerstarsse 5, CH-3012 Bern, Switzerland*

Ilia Britvitch, Andrei Kouznetsov, Yuri Musienko, Stephen Reucroft and John Swain,
*Northeastern University, Boston, USA*

W. Chen, Z. Li (co-spokesman)
*Brookhaven National Laboratory, Upton, NY 11973-5000, USA*

C. Da Viá
*Brunel University, Uxbridge, Middlesex UB8 3PH, UK*

L. Casagrande[1], S. Grohmann[2], E. Heijne, C. Lourenço, T.O. Niinikoski, G. Nuessle and B. Perea Solano
*CERN, CH-1211 Geneva, Switzerland*

O. Hempel, R. Herzog and E. Wobst
*ILK Dresden, Bertolt-Brecht-Allee 20, 01309 Dresden, Germany*

E. Borchi, M. Bruzzi, D. Menichelli and S. Pirollo
*Dipartimento di Energetica, Universitá di Firenze, I-50139 Firenze, Italy*

Y. Popowski
*Department de Radiologie, Universite de Geneve, CH-1211 Geneva, Switzerland*

R. Bates, C. Buttar,V. O'Shea, C. Parkes
*Department of Physics and Astronomy, University of Glasgow, Glasgow G12 8QQ, UK*

J. Härkönen (co-spokesman), P. Luukka, E. Tuominen and E. Tuovinen
*Helsinki Institute of Physics, P.O.Box 64, 00014 University of Helsinki, Finland*

W. de Boer, H. Bol, A. Dierlamm, A. Furgeri, E. Grigoriev[3], F. Hauler and L. Jungermann
*IEKP University of Karlsruhe, D-76128 Karlsruhe, Germany*

M. Abreu, P. Rato Mendes, P. Sonderegger and P. Sousa
*LIP, Av. E. Garcia, P-1000 Lisbon, Portugal*

V. Cindro, I. Mandic, M. Mikuz and M. Zavrtanik
*Jozef Stefan Institute, Exp. Particle Physics Dep., PO Box 3000, 1001 Ljubljana, Slovenia*

O. Militaru, K. Piotrzkowski and X. Rouby
*Université Catholique de Louvain, B-1348 Louvain-la-Neuve, Belgium*

Rita De Masi and S. Paul
*Physik Department E18, Technische Universität München, D-85748 Garching, Germany*

S. Buontempo, N. D'Ambrosio and S. Pagano
*Dipartimento di Fisica, Universitá "Federico II" and INFN, I-80125 Napoli, Italy*

V. Eremin, I. Ilyashenko and E. Verbitskaya
*Ioffe Physico-Technical Institute, Russian Academy of Sciences, St. Petersburg 194021, Russia*

R. Laiho, L. Vlasenko[4] and M. Vlasenko[5]
*University of Turku, Wihuri Physical Laboratory, FI-20014 Turku, Finland*

P. Anbinderis, T. Anbinderis, E. Gaubas, V. Gorbatenko, V. Kalesinskas, J. Kapturauskas and  J. Vaitkus
*University of Vilnius, Institute of Materials Science and Applied Research, 2040 Vilnius, Lithuania*

---

[1] Now at INFN, Section of Rome II, Italy
[2] Now at SINTEF, Trondheim, Norway.
[3] Also at Department de Radiologie, Geneva Switzerland
[4] Also at Ioffe PTI, St. Petersburg, Russia

# Summary

CERN RD39 Collaboration is working for development of super-radiation hard cryogenic Si detectors for applications for LHC experiments and their future upgrades. Radiation hardness up to $10^{16}$ $n_{eq}/cm^2$ is required in the future HEP experiments. The main measure detector's radiation hardness is the Charge Collection Efficiency (CCE), which is affected by both the detector sensitive volume (depletion depth) and charge trapping by radiation-induced trapping centers. However, $10^{16}$ $n_{eq}/cm^2$ fluence is well beyond the radiation tolerance of even the most advanced semiconductor detectors fabricated by commonly adopted technologies: a) the full depletion voltage will be in the thousands of volts for a 300 µm thick Si detector operated at or near room temperature (RT), and b) at this radiation load the carrier trapping will limit the charge collection depth to an effective range of 20 µm to 30 µm regardless of depletion depth. To improve the detector overall CCE, one has to solve both problems a) and b) simultaneously.

Significant improvement of the radiation hardness of silicon sensors has been taken place within RD39 during the past years. Fortunately the cryogenic tool we have been using provides us a convenient way to solve the detector CCE problem at SLHC radiation level ($10^{16}$ $n_{eq}/cm^2$). There are two key approaches in our efforts: 1) use of the charge/current injection to manipulate the detector internal electric field in such a way that it can be depleted at a modest bias voltage at cryogenic temperature range ($\leq 150K$); and 2) freezing out of the trapping centers that affects the CCE at cryogenic temperatures lower than that of the $LN_2$ temperature.

In our first approach, we have developed the advanced radiation hard detectors using charge or current injection, the current injected diodes (CID). In a CID, the electric field is controlled by injected current, which is limited by the space charge, yielding a nearly uniform electric field in the detector, independent of the radiation fluence. Different modes of current or charge injection was studied: 1) Charge injection mode using a LED or laser as light source; 2) Ohmic current injection mode using the symmetric $p^+$-n-$p^+$ structure (after radiation beyond space charge sign inversion it becomes $p^+$-p-$p^+$; and 3) Forward current injection mode using the p/n/n junction diode structure operated at forward bias potential. It was found that internal electric field can be greatly modified in CID detectors, and CID detectors can be operated in the temperature range of 100 K to 200 K with much improved CCE (due to this field modification) as compared to RT operation. In our second approach, we have developed models of radiation-induced trapping levels and the physics of their freezing out at cryogenic temperatures. Future studies are now under way to build the detector CCE measurement system using ultra-fast picosecond laser and electron source with LHe cryostat to find the practical cryogenic temperature range that can be used to freeze out the radiation-induced trapping levels.

# 1  INTRODUCTION

Significant advances have been made by the CERN RD39 Collaboration in obtaining super-radiation hard cryogenic silicon detectors for applications in experiments in LHC and its future upgrades. Our approach differs from the traditional methods for improvement of silicon radiation detectors, which are based on the modification of the properties of silicon by doping with different impurities or lattice defects [1]. The best results were achieved for silicon doped with oxygen, e.g. Czochralski silicon (Cz-Si) [2], or silicon doped by the long-term oxidation [3]. The maximum improvement of the radiation hardness is by a factor of 2-3 for protons, but little improvement is revealed for neutron-irradiated detectors [4, 5]. Detectors fabricated from novel materials, such as diamond and SiC, still face problems in detector processing, high cost of material and polarization under severe irradiation. Detailed modeling of the Lazarus effect [6] has shown that detector electric field in irradiated Si detectors can be manipulated by the filling status of two deep defect levels at cryogenic temperatures. Furthermore, advanced radiation hard detectors using charge/current injection, or the charge/current injected diode (CID), have been developed by RD39. In a CID, the electric field is controlled by the space charge current limited mode. Irrespective of the radiation fluence, the internal electric field is nearly uniform if the detector is operated in charge/current injection mode. Charge/current injections in different modes have been studied: 1) charge injection mode using a LED or laser as light source; 2) Ohmic current injection mode using the symmetric $p^+$-n-$p^+$ structure (after radiation beyond space charge sign inversion it becomes $p^+$-p-$p^+$; and 3) forward current injection mode using the p/n/n junction diode structure operated at forward bias voltage. The key of our approach is to use freeze-out of the trapping that affects Charge Collection Efficiency (CCE). Temperatures lower than the 80 K may be needed here.

The deterioration of CCE due to the trapping of charge carriers is a severe obstacle for the use silicon sensors in future very high luminosity colliders. The particle radiation induces trapping centres that eventually leads to the reduction in the signal height, produced by MIPs (minimum ionising particles). In the LHC bunch-crossing interval is 25 ns and the trapping is generally considered rather insignificant, but obviously it will become a major issue if in the possible LHC upgrade the bunch-crossing interval is reduced to 10 ns [7].

The detector CCE can be considered to be a product of two factors [8].

$$CCE = CCE_{GF} \cdot CCE_t = \frac{w}{d} \cdot e^{-t_{dr}/\tau_t} \ , \qquad (1)$$

where $w$ is the depletion depth, $d$ the detector thickness, $\tau_t$ the trapping time constant, and $t_{dr}$ the carrier draft time. In Eq. 1, $CCE_{GF}$ is a geometrical factor that is affected by detector full deletion voltage $V_{fd}$ (or effective doping concentration $N_{eff}$) via the relations:

$$w = \sqrt{\frac{2\varepsilon\varepsilon_0 V}{eN_{eff}}} \ \text{ and } \ \frac{w}{d} = \sqrt{\frac{V}{V_{fd}}} \qquad , (2)$$

where $e$ and $\varepsilon$ have their usual meanings. The second term $CCE_t$ in Eq. 1 is the trapping factor that is related to the trapping of carriers by defects.

The trapping ($\tau_t$) and detrapping ($\tau_d$) time constants for a trap level can defined by:

$$\begin{cases} \tau_t = \dfrac{1}{\sigma v_{th} N_t} \\ \tau_d = \dfrac{1}{\sigma v_{th} N_C e^{-E_t/kT}} \end{cases} \qquad (3)$$

where $\sigma$ is the capture cross section of the trap, $v_{th}$ is the thermal velocity of charge carriers, $N_T$ is the concentration of traps, $N_C$ the electric state density in the conduction band, and $E_t$ the trap energy level in the band gap.

The trapping time constant is nearly independent on temperature (or weak dependence on $T$). However, it depends strongly on the radiation fluence $\Phi_n$. The elevated depletion voltage of heavily irradiated silicon detectors is due to various radiation -induced defects. Two deep levels, however, are recognized to be most responsible for the increase of the effective doping concentration and adopted as basis of the modeling of radiation effects [9-12]. These experimentally observed levels are a deep donor (DD) 0.48 eV above the valence band and a deep acceptor (DA) 0.527 eV below the conduction band. The capture cross section of both levels is approximately $10^{-15}$ cm$^2$. Presumably because of the introduction above-mentioned DD and DA levels, a hadron irradiation of Super-LHC like fluence would give rise for very high $N_{eff}$. For example, in recently developed, very high oxygen concentration, high resistivity magnetic Cz-Si detectors the $N_{eff}$ increases up to $3$-$5*10^{13}$ cm$^{-3}$ after $10^{16}$ n$_{eq}$/cm$^2$ (n$_{eq}$: 1 MeV neutron equivalent) irradiation [13]. A 200 $\mu$m thick Cz-Si detector could still be fully depleted below 1 kV operating voltages. Due to the saturation of thermal velocity at about $10^7$ cm/s value, the trapping time constant would, however, limit the collection of charge carriers within 20-30$\mu$m depth in the bulk, thus 80-90% detectors volume would represent an effective dead space.

As demonstrated by the previous RD39 results [14], the $CCE_{GF}$ can be increased close to 1 by manipulating the electric field in the detector via current and/or charge injection at temperatures from 130 K to 150 K. Since for fluence less than$10^{15}$ n/cm$^2$, the trapping term $CCE_t$ is insignificant, CCE can be significantly improved by improving only the $CCE_{GF}$ at temperatures from 130 K to 150 K. This is in fact the original "Lazarus" effect. However, for extremely high fluence ($10^{16}$ n/cm$^2$) in LHC upgrade environment, the trapping term can also be significant and affect the CCE greatly. The approach of RD39 to overcome the fundamental trapping problem at very high fluencies is to modify the $CCE_t$ at the low temperatures. Temperatures lower than the 80 K may be needed here.

As can be seen in Eq. 3, the detrapping time constant depends very strongly on the temperature. This dependence makes it possible to freeze out trapping centers at low temperatures. If a trap level is filled (say, by current or charge injection) and then frozen (very long detrapping time, see Eq. 3) at cryogenic temperatures, this trap level will no longer be able to trap free carriers again, and it becomes electrically inactive. In this case, the $CCE_t$ can be improved as well to a value close to 1, and therefore significantly improve the CCE.

Since some trap levels are shallow, one has to go to cryogenic temperatures to freeze them out. In addition to deep DA and DD, a well-known, shallow radiation-induced trapping center in Si, is the so called A-center (O-V) at $E_c$-0.18 eV with capture cross section of $10^{-15}$ cm$^2$ [15]. For the A-center, the detrapping time constants at various temperatures are listed in Table I.

Table I. Detrapping time constant for the A-center at various temperatures

| T(K) | $\tau_d$ |
|------|----------|
| 300 | 10 ps |
| 150 | 10 ns |
| 100 | 10 µs |
| 77 | 6 ms |
| 60 | 12 s |
| 55 | 5 min |
| 50 | 3.6 h |
| 45 | 15 days |
| 40 | 13 years |

It is clear that already the A-center is freezing out for 10's of seconds at T=60 K. At T=45 K, the A-center will be frozen for 15 days after filling, and for 13 years at T=40 K. So if one fills the A-center at T=40 K, it will not be active as trapping center for the next 13 years! Even at higher temperatures, sat at T=45 K, one may need to fill the A-center every 15 days, which can easily be done.

## 2   CURRENT INJECTION TO HEAVILY IRRADIATED SILICON DETECTORS

In this content, RD39 proposes a new approach for detector operation. This concept is based on current injection to the detector's active volume. The first publications on the application of current injection to the detector bulk for improvement the performance of heavily irradiated detectors [16, 17] were focused on the manipulation of the electric field distribution by light generated carriers. It was shown that the optimal density of the injected current allows adjustment of the electric field to nearly uniform distribution and the corresponding reduction of the detector full depletion voltage from several hundreds to several tens of volts. However, the optimal injected current should be adjusted to the certain fluence that requires its progressive increase with the fluence accumulation. In the considered new approach the detector operates in the mode of "self-limited injected current", which maintains automatically a stable electric field distribution in the detector at any fluence.

## Samples

The simplest structure of Current Injected Detector (CID) with self-limited injected current is a symmetric $p^+$-n-$p^+$ or $p^+$-p-$p^+$ structure based on the n-type or p-type bulk material. The initial doping in these devices has been compensated by deep levels. The deep levels can be intentionally introduced during the detector processing (by doping of impurities with deep energy levels or using thermal treatments), or simply by irradiation. In our study the CIDs were processed on high resistivity FZ Si wafers with a resistivity of 5-7 kOhm·cm and a thickness of 350-400 μm. The detector active area was 10– 25 mm$^2$. Additionally, a set of irradiated regular $p^+$-n-$n^+$ detectors processed from different types of silicon (FZ, 5-7 kOhm·cm, MCz, 1 kOhm·cm) with close geometrical sizes was used at forward biased mode [18]. In order to reveal the possible influence of the detector processing technology on the CID operation, the devices were selected from the batches processed at different institutes: Brookhaven National Laboratory (USA), Research Institute of Material Science and Technology (Russia), Helsinki Institute of Physics (Finland). The detectors were irradiated by neutrons with fluence in the range $5 \cdot 10^{14}$–$3 \cdot 10^{15}$ $n_{eq}$/cm$^2$. The detector IV characteristics were measured in dry nitrogen in the temperature range 180-250 K.

## Experimental results and discussions

IV characteristic of $p^+$-n-$p^+$ current injected detector irradiated by a fluence of $1 \cdot 10^{15}$ $n_{eq}$/cm$^2$ and operated at 200 K is shown in Fig. 1. Three parts can be distinguished in the IV curve: a nearly linear region with a slope close to 1 in the range of low bias (3-40V), a region with a slope of about 2 in the medium bias range (40-200V), which transfers to the region of a sharp current increase. The similar IV curves were observed for regular $p^+$-n-$n^+$ irradiated detectors. Reproducibility of IV characteristics, with respect to the measurement conditions, was checked in the measurement with increasing and decreasing bias voltage and no hysteresis was observed.
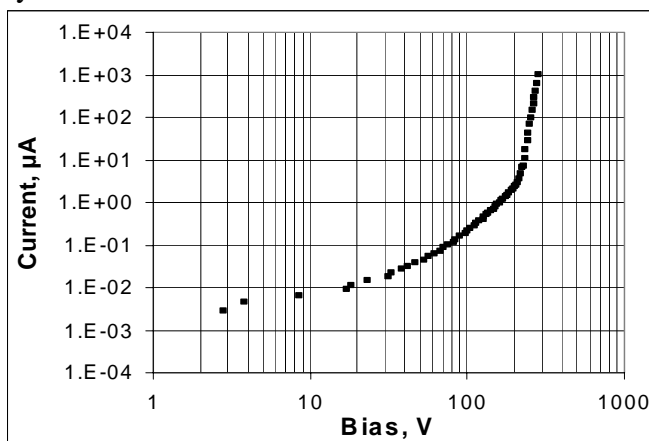


Fig. 1. IV curve for $p^+$-n-$p^+$ detector irradiated by a fluence of $1 \cdot 10^{15}$ $n_{eq}$/cm$^2$ at the temperature of 200 K.

Our model for CID operation at self-stabilized current injection (SSCI) is based on the analysis of current flow in heavily doped insulators [19]. In symmetric structure under applied bias the holes are injected into the detector volume from one of the $p^+$ contacts. The

injected holes are trapped to the deep levels in the detector bulk that changes the space charge density and the electric field distribution. The steady state density of the trapped charge is the balance between the trapping and detrapping rates. Both rates depend on the concentration of the injected carriers. It is clear that the local value of $N_{eff}$ will increase with the increase of the injected free carrier density or the current value. A general feature of the position dependent space charge concentration ($N_{eff}(x)$) is that the trapped charge carriers will reduce the electric field near the injecting contact. This trend is illustrated in Fig. 2, from [17]. Obviously that at certain value of the injected current, the electric field ($E(x=0)$ or $E_{inj}$) will reach the value close to zero. At these conditions the increase of the injection current density $J_{inj}$ will be limited by the low electric field and remains stable. This mode is known as a Space-Charge-Limited Current (SCLC) mode and it has been observed earlier in insulators [19].

The solution of the continuity and Poisson equations using the Shockley–Read –Hall statistics for carriers trapped by the deep levels gives the trapped charge density distribution. Fig. 2 and 3 show the calculated $N_{eff}(x)$ and $E(x)$ for the $p^+$-n-$p^+$ structure for the deep level trapping center with the activation energy $E_t – E_V = 0.48$ eV and the concentration of $N_t \approx 2.8 \cdot 10^{12} cm^{-3}$.

The important feature of $E(x)$ is that the electric field extends over the entire thickness, which means detector is fully depleted. The electric field has a maximum at the contact opposite to the injecting contact, and its value depends only on the detector thickness $d$ and the bias voltage $V$. As CID operation mode the $E(x)$ profile is independent on the material properties, no sensitivity to radiation influence is expected.

The calculated $E(x)$ distribution at $V = 30$ V (Fig. 3) well illustrates that the detector is fully depleted, whereas without injection the depth of the space charge region is 120 μm, only limited by the concentration of electrically active deep levels of $2.8 \cdot 10^{12} cm^{-3}$. This effective trap concentration is resulted by the irradiation with approximately $5*10^{14} n_{eq}/cm^2$.
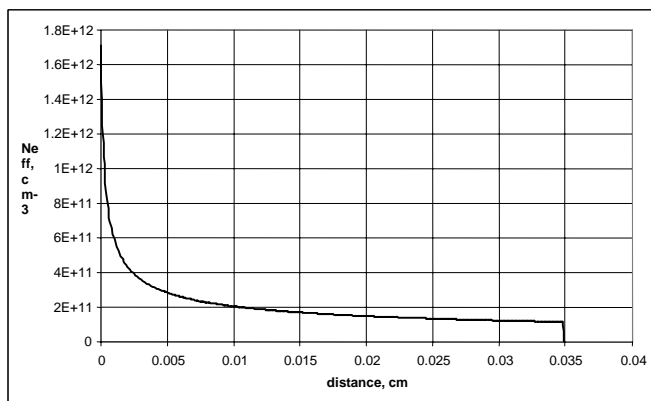


Fig. 2. Effective concentration calculated for CID with hole injection at: $J_{inj} = 1 \cdot 10^{-5}$ A/cm$^2$, V=30 V, $N_{dl}=2.8 \cdot 10^{12} cm^{-3}$

Fig. 3. Electric field distribution calculated for CID with hole injection at: $J_{inj} = 1 \cdot 10^{-5}$ A/cm$^2$, V = 30 V, $N_{dl} = 2.8 \cdot 10^{12}$ cm$^{-3}$

The IV characteristic of the CID operating at SSCI mode and calculated with the same parameters as those for Figs. 2 and 3 is shown in Fig. 4. The SSCI mode defines specific IV characteristic with three major features: the linear (ohmic) IV dependence at low current, square IV dependence at the SCLC mode for the major region of IV curve, and a sharp current rise at a certain bias voltage. The Ohmic part corresponds to a low injected current density, which cannot disturb the free currier concentration in the detector bulk material. The quadratic part is a space charge limited current with the concentration of the injected curriers $n>>n_0$. The sharp current rise is a result of the deep level trap saturation when all traps are completely filled. This saturation prevents further self-adjustment of the trapped charge density to the bias. In this case any increase of bias will lead to non-limited current injection until the injected free carriers itself start to influence on the electric field distribution. This will require $n>N_t$. It should be emphasized that the sharp rise of the current is not related to any breakdown effects.
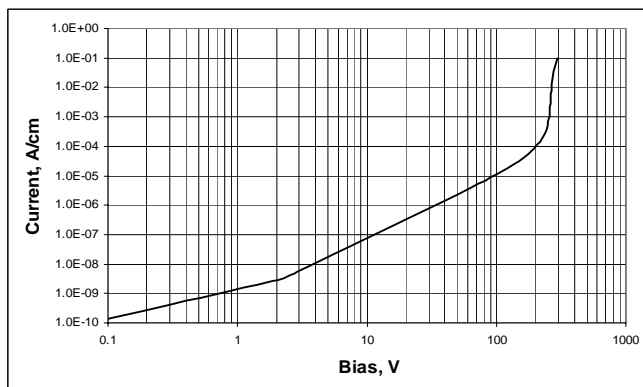


Fig. 4. Calculated IV characteristic for CID. Parameters for calculation are the same as in Figs. 2 and 3.

Fig 5 presents IV characteristics of irradiated p$^+$-n-n$^+$ structures, which show the same behavior as that for p$^+$-n-p$^+$ detector presented in Fig. 1. The only difference is that the ohmic region of the IV curves in Fig. 5 is hardly visualized due to parasitic leakage current. The threshold voltage $V_{thr}$ corresponding to the sharp current rise is only slightly affected by

temperature. The IV curves simulated with the same activation energy of the deep donor, $E_t - E_v = 0.48$ eV, and $N_{dl}$ close to $2.8 \cdot 10^{12}$ cm$^{-3}$ fit well to the full set of the experimental curves. This concentration was only slightly adjusted to fit the threshold voltage. The capture cross-section for electrons and holes was equal to $1 \cdot 10^{-15}$ cm$^2$.
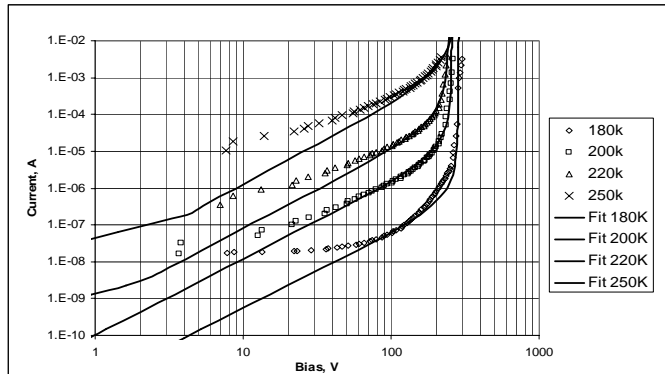


Fig. 5. Experimental and simulated IVs of CID irradiated by a fluence of $1 \cdot 10^{15}$ n$_{eq}$/cm$^2$ operated at different temperatures.

The used set of parameter for the deep donor corresponds to the parameters of the mid-gap deep donor that was defined earlier as one of the two mid-gap levels responsible for operational characteristics of heavily irradiated Si detectors [20, 21]. The mid-gap deep donor at $E_t - E_v = 0.48$ eV is most influential trap for holes. The observed behavior of IV curves is a direct proof that heavily irradiated detectors with hole injection operate at self-stabilized current mode.

One important point for CID application is the range of the operational bias and the value of operational or leakage current. Fig.6 presents the set of IVs for CID irradiated by different neutron fluencies. The detectors were processed on n-type MCZ high resistivity silicon wafers with thickness of 300 μm at PTI. The experimental IVs were simulated with the deep level trapping centers used above. The parameter, which was only adjusted, is the concentration of trapping centers $N_t$.
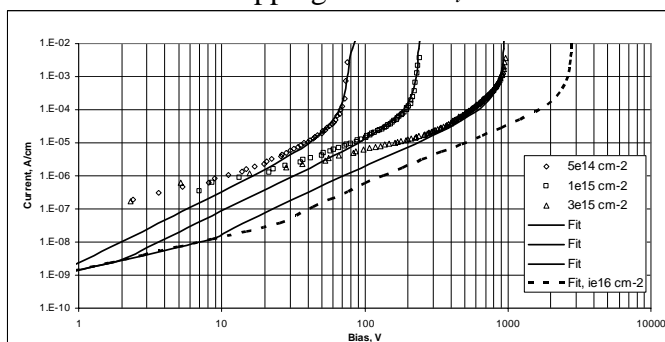


Fig. 6. Experimental and simulated normalized IVs of CID irradiated by different fluencies and operated at 220 K.

The value of $N_t$ used for the fit is nearly linearly depend on fluence with coefficient of about $dN_t/dF=2.5 \cdot 10^{-2}$ cm$^{-1}$. This parameterization allows to calculate the IVs at F$>1 \cdot 10^{16}$ cm$^{-2}$, which presented in Fig. 6 as a dashed line.

The major trend of the IV curves changes with fluence is increase of the threshold voltage at which the current starts rise fast. This trend is well demonstrated in Fig. 7 where $V_{thr}$ is plotted as a function of neutron fluence.
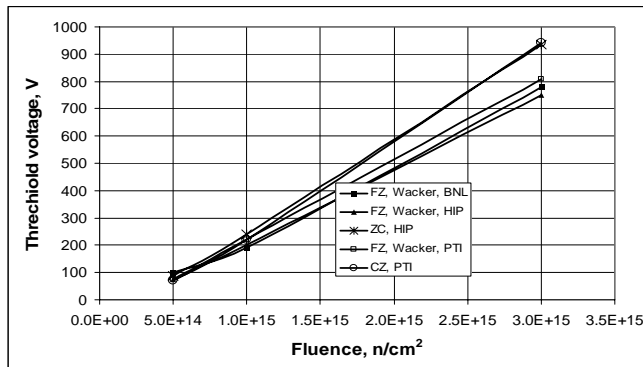


Fig. 7. Dependence of threshold voltage on irradiation fluence for current injected detectors processed from different types of Si and at different facilities

The threshold voltage linearly increases with fluence with the coefficient $dV_{th}/dF = 2.5 \cdot 10^{-13}$ V·cm$^{-2}$. For the expected maximal SLHC fluence of $3 \cdot 10^{15}$ cm$^{-2}$ it is near 1000 V. This value is far above the operational voltage of 300 V defined for the ATLAS inner tracker detectors.

In regular detectors the bulk generated current increases with fluence with the rate of $4 \cdot 10^{-17}$ A/cm for 1 MeV neutron irradiation. This rate leads to the leakage current of $1.2 \cdot 10^{-3}$ A/cm$^2$ for 300 μm thick detector irradiated up to fluence of $1 \cdot 10^{15}$ cm$^{-2}$. Comparison of this value with the current for CIDs shows that this value is very close to the current at the threshold voltage, which is a maximum value in the operational range. Therefore we expect the CID leakage current lower that those for the regular detectors that confirms by experimental date. For example, at fluence $1 \cdot 10^{15}$ cm$^{-2}$ the optimal bias voltage is about 150V that gives current less then $1 \cdot 10^{-4}$ A/cm$^2$.

The important advantage of CID is that at certain value of the bias the current reduces with fluence. The increase of fluence from $1 \cdot 10^{15}$ cm$^{-2}$ to $3 \cdot 10^{15}$ cm$^{-2}$ for the CID biased at 200V leads to current reduction of about 1 order of the magnitude. This is a unique feature of CIDs, which must be better studied.

To define the influence of different types of Si and the detector technology on the CID performance, the set of detectors irradiated by the same neutron fluence of $1 \cdot 10^{-15}$ cm$^{-2}$ was evaluated at T = 220 K. For all detectors similar self-stabilized injection current is observed and the detector IV characteristics are very close to each other in major details (Fig. 8).
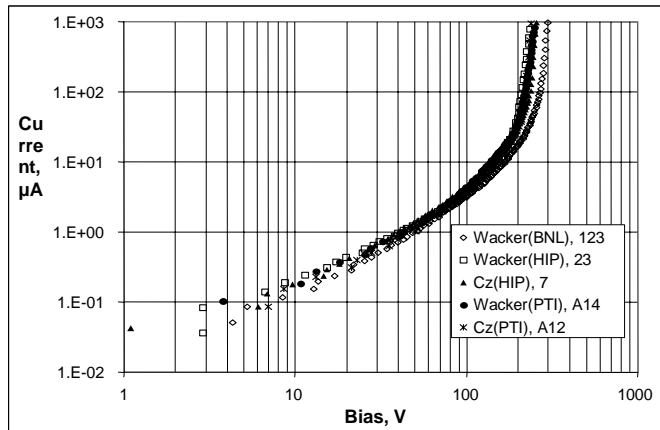
Fig. 8. IV characteristics of CIDs irradiated by neutron fluence of $1 \cdot 10^{15}$ cm$^{-2}$ measured at T = 220 K. The detector active area is 0.25 cm$^2$.

This observation allows concluding that:

a)  in any type of silicon and for any detectors technology the concentration of deep traps, which controls the SCLC, is a function of the fluence and is not affected by the material properties and the technology;

b)  the range of operational bias is limited by the $V_{thr}$, which is 200 V at neutron fluence of $1 \cdot 10^{15}$ cm$^{-2}$;

c)  the operational injected current for detectors irradiated by neutron fluence of $1 \cdot 10^{15}$ cm$^{-2}$ and operated at 220 K  is about of 0.1 mA/cm$^2$ that fits to the requirements for readout electronics with shaping time less than 20 ns expected for future upgrades of LHC experiments.

The other detector parameter influenced by irradiation is the charge collection efficiency (CCE). It value defined by the concentration of deep levels actively trap the collected charge carriers. The mostly active traps are the charged deep levels, which have trapping cross-section in the range of $1 * 10^{-14} - 1 * 10^{-15}$ cm$^2$ for the opposite charged carriers (attractive centers). In case of neutral centers the cross-section is of one order of magnitude smaller and therefore their contribution to the CCE reduction is not essential. RD39 expects that CIDs operation at SSCI mode will give additional advantage for detector operation as the injected carriers which re trapped by trapping centers will reduce the concentration of the charged traps and therefore the CCE decrease rate with fluence will be low.

The performed study shows that silicon p$^+$-n–n$^+$ and p$^+$-n– p$^+$ detectors heavily irradiated by neutrons operate in SCLC mode with hole injection. The threshold voltage and the dark current of CIDs are in the range of hundreds volts and 100 μA/cm$^2$, respectively, which fits to the detector application requirements for future SLHC. The CIDs IV characteristics are stable under irradiation and the operational bias range increases with fluence. The CID technology developed with pre-irradiation by neutrons is insensitive to the type of high resistivity silicon.

CID engineering allows proper simulation of IV characteristics with well defined physical parameters of deep traps and expected irradiation fluence.

# 3   CHARGE COLLECTION EFFICIENCY (CCE) MEASUREMENTS WITH LASER INJECTION

It has been shown in previous Chapters [22,23] that the space charge in irradiated detectors can be manipulated with carrier injection. This represents one possible method for lowering the depletion voltage, as has been proposed in Ref. [24]. Another approach is to operate heavily irradiated detectors under forward bias [25,26]. Both methods can reduce the problem of high operating voltages, however, a consequence of this is that the detector current is substantially increased and this influences the noise performance. The current increase can, however, be limited by decreasing the operating temperature. The operation of irradiated silicon detectors under continuous carrier injection has been studied in detail in Refs. [23,27,28]. Continuous (DC) light illumination of one detector side with light of a short penetration depth enhances the free electron or hole concentration in the active volume of the detector, which influences the occupation probability of traps. Charged traps contribute to the space charge in an irradiated detector. Modification of the space charge can reduce the voltage needed to establish the electric field throughout the whole detector thickness. TCT studies with a red laser at $T \approx -10^0C$, described in Ref. [23], have shown that the concentration of negative space charge in irradiated detectors can be reduced by continuous hole injection and therefore full depletion can be reached at lower bias voltages. However, the measurements in Ref. [23] were made with detectors irradiated up to $2*10^{14}$ n/cm$^2$, which is the relevant radiation level for strip detectors in the LHC experiments, and only predictions were made about the possibility of using this method at higher fluencies. In this study we report measurements of the charge-collection efficiency (CCE) with a $^{90}$Sr source in detectors irradiated up to $8*10^{15}$ n/cm$^2$, which are the radiation levels relevant for future experiments such as those at the upgraded LHC. As already mentioned, a promising method of extending the usability of silicon detectors to fluencies beyond $10^{15}$ n/cm$^2$ is operation under forward bias. This method is particularly beneficial when operating at low or cryogenic temperatures because of the smaller current increase [29,30]. In the next sections, measurements of the CCE under forward bias in the temperature range from -180 to $-30^0C$ are presented and compared with measurements at reverse bias with an increased free-carrier concentration.

## 3.1 Samples and measurement setup

The measurements were made on a set of four pad detectors (diodes) with a 0,5 X 0,5 cm$^2$ surface and a 300 μm thickness. The detectors have mesh metallization on the n-side and a hole in the metallization on the p-side. The diodes were processed by ST Microelectronics on standard Fz-Si wafers from Wacker with an initial resistivity of 15 kΩcm. The silicon crystals were cut along the <111> plane. The samples were irradiated with neutrons in the TRIGA nuclear reactor of the Jozef Stefan Institute in Ljubljana [31,32] to the following 1 MeV neutron NIEL equivalent fluencies: $5*10^{14}$, $1*10^{15}$, $4*10^{15}$ and $8*10^{15}$ n/cm$^2$. After irradiation the samples were kept at room temperature for two weeks to anneal to the minimum in full depletion voltage and then stored at $-17^0C$. The measurements were made with diodes

mounted in a temperature-controlled liquid-nitrogen cryostat (Janis VPF-100 LN2) that allows the temperature to be varied between -190 and –30$^0$C with 0,2$^0$C stability. The sample mounted inside the cryostat was connected to the rest of the readout system with a coaxial cable. A Picosecond PulseLab 5532 Bias-T was used to supply the bias to the sample from a Keithley 2410 I–V meter, which was also used for measurements of the detector current. The signals were amplified with a MITEQ AM-1309 wide-band current amplifier and digitized with a Tektronix TDS 754 C digital oscilloscope triggered by a photomultiplier (PMT) connected to a scintillator. A set of collimators in front of the scintillator selected electrons from the $^{90}$Sr source traversing the detector. The trigger rate was around 5 events per second. During the measurements with an increased free-carrier density the detector surface was illuminated by DC light ($\lambda$=633 nm) from a laser source through the cryostat window.

### 3.2 Temperature scans

   The obvious method to reduce the current in an irradiated detector is to reduce the operating temperature. In Fig. 9, measurements of current vs. temperature for diodes irradiated to different fluencies are shown. Sensitivity of the current measurements was 10$^{-8}$A and the variations in the currents in Fig. 6, which are smaller than $\approx$10$^{-7}$ A, are within precision of the measurement.
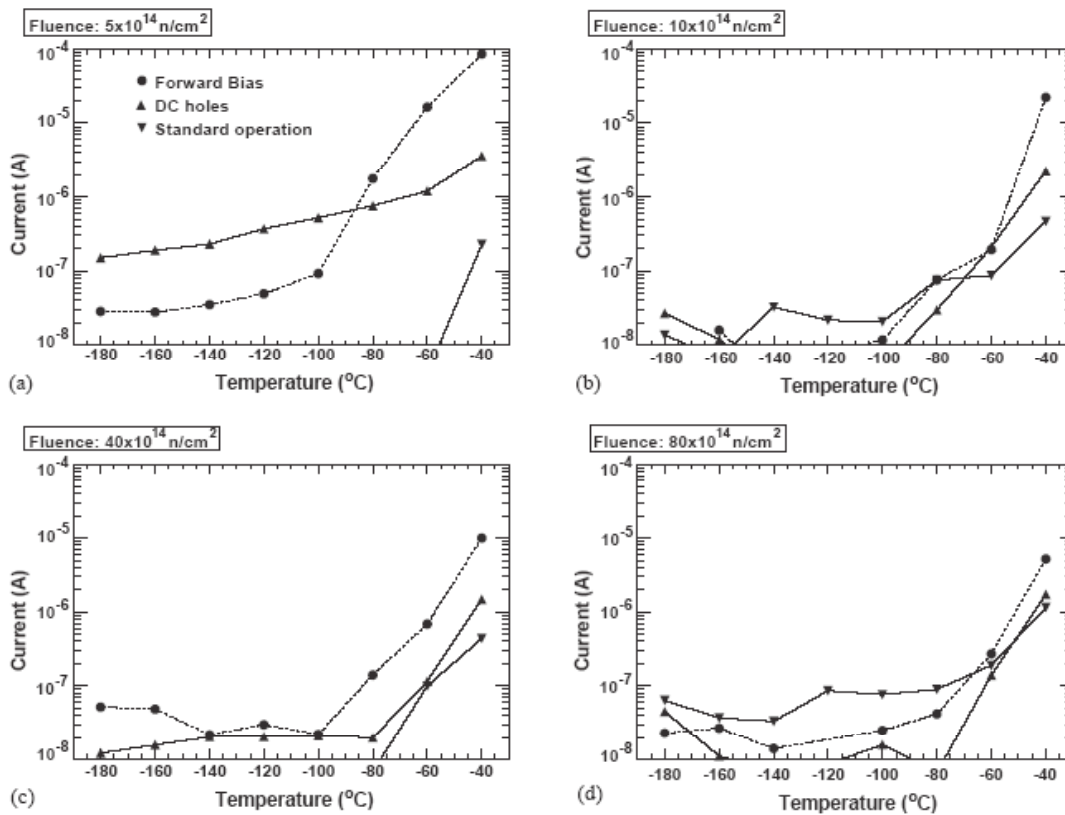
Fig. 9. Current dependence on temperature for diodes irradiated to equivalent fluences of (a) $5*10^{14}$ n/cm$^2$, (b) $1*10^{15}$ n/cm$^2$, (c) $4*10^{15}$ n/cm$^2$ and (d) $8*10^{15}$ n/cm$^2$. DC hole injection and standard operation measurements were made at a reverse bias of 250 V. Forward bias measurements were done at 80V in (a), 120V in (b) and at 250V in (c) and (d). The description of the symbols in (a) is also valid for the other three plots. The sensitivity of the measurements is $10^{-8}$ A.

It is clear that cooling reduces the currents in all modes of operation. One should note that also in the DC-light illumination mode the detector current is reduced at lower temperatures, although the intensity of the illumination is not changed. This effect is in agreement with following hypothesis: at lower temperature a smaller free-hole concentration is needed to re-invert the space-charge sign of the irradiated detector [23] because of the longer detrapping times. Therefore, a low electric field condition at the n$^+$ contact is reached at a lower additional current.

Scans of CCE were made in the temperature range from -180 to –40$^0$C in four different modes of operation: forward bias, DC hole injection (n-side illumination), DC electron injection (p-side illumination) and standard operation. Fig. 10 shows the results of the measurements.
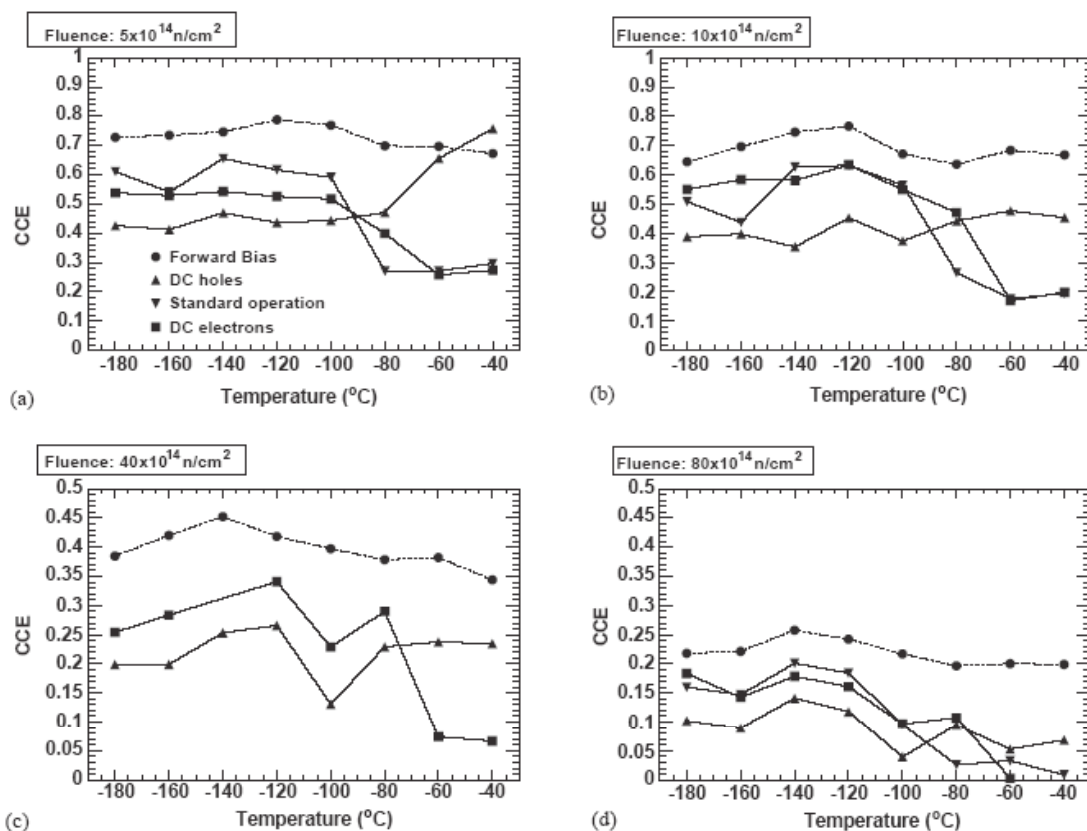


Fig. 10. CCE vs. temperature for diodes irradiated to equivalent fluencies of (a) $5*10^{14}$ n/cm$^2$, (b) $1*10^{15}$ n/cm$^2$, (c) $4*10^{15}$ n/cm$^2$ and (d) $8*10^{15}$ n/cm$^2$. DC hole injection, DC electron injection and standard operation measurements were made at a reverse bias of 250 V. Forward bias measurements were made at 80V in (a), 120V in (b) and at 250V in (c) and (d). The description of the symbols in (a) is also valid for other three plots.

All the measurements were made with detectors biased all the time during the measurements (a full temperature scan from -180 to –40$^0$C takes a few hours). For

measurements in the standard mode of operation the samples were not completely shielded from the ambient light. So standard mode of operation means a reverse bias without DC laser illumination, but with some exposure to ambient light. At low temperatures the polarization of the detectors [6] also occurs at very low light intensities. Therefore, a comparison with other CCE measurements at low temperatures reported in the literature, made either in the stable state or immediately after bias switch-on, but completely shielded from any light, should be undertaken with care. It is clear from Fig. 10 that at temperatures below $60^0$C the highest CCE is measured with forward bias operation. CCE measured in this mode of operation also does not depend much on the temperature since the variations seen in Fig. 10 are within the precision of the measurement. An increase of the CCE with cooling can be seen in the standard mode of operation or with the DC electron injection, with the transition from low to high CCE occurring in the temperature interval from -60 to $–100^0$C. At the lowest fluence ($5*10^{14}$ n/cm$^2$) the decrease of the CCE with cooling in the same temperature interval is also measured in the DC hole-injection mode. At temperatures below $90^0$C the lowest CCE is measured in the DC hole-injection mode at all fluencies. The variations of the CCE below $–90^0$C are within the experimental uncertainties. The transitions of the CCE from low to high under reverse-bias modes of operation can qualitatively be explained by space-charge sign inversion occurring in this temperature interval. Namely, with a negative space charge at high temperatures DC hole injection is beneficial because it reduces the total space charge and increases the depletion depth. Similarly, the injection of electrons at low temperature reduces the positive space charge, which results in a larger depletion depth. The increase of the CCE observed in the standard mode of operation indicates that space charge concentration decreases with falling temperature. The transitions of CCE shown in Fig. 10 occur in the same temperature range as the transitions of the CCE and space charge sign reported in Ref. [33].

### 3.3 Modeling

An attempt was made to interpret the measured results with a simple model. Signals were simulated assuming the uniform creation of charge through the detector depth. The created charge was divided into buckets, each corresponding to 1μm of track. The induced current was calculated for each bucket by drifting it through the electric field using Ramo's theorem [34] with a 1/D weighting field assumed. The sum of the signals caused by all buckets yields the induced current and is calculated separately for electrons $i_e(t)$ and holes $i_h(t)$. These are multiplied by the corresponding trapping factors $exp(-t/\tau_e)$ and $exp(-t/\tau_h)$, where $\tau_e$, $\tau_h$ are the effective trapping times for the electrons and holes, respectively. The collected charge was obtained by integrating the current pulse over 18 ns. The details of the signal simulation are explained in Ref. [35].

The effective space-charge concentration and trapping times were calculated considering two dominant deep levels. The contribution of a defect to the space-charge concentration $Q$ is given by

$$Q = e_0 N(k - P) = e_0 g \Phi_{eq}(k - P) \qquad (4),$$

where *k=0,1* for acceptors and donors. The *P* is the occupation probability, *N* is the concentration, *g* is the introduction rate of the deep trap and $\Phi_{eq}$ the equivalent neutron fluence. The effective trapping times for electrons and holes were obtained from

$$\frac{1}{\tau_e} = v_{th,e}\sigma_e(1 - P_e)g_e\Phi_{eq} \qquad (5),$$

$$\frac{1}{\tau_h} = v_{th,h}\sigma_h P_h g_h \Phi_{eq} \qquad (6),$$

where $P_e$ is the occupation probability of the dominant electron trap (acceptor) and $P_h$ is the occupation probability of the dominant hole trap (donor). The occupation probability *P* of a defect is calculated using equations from [24,36]

$$P = \left[\frac{c_p p + c_n n_i \chi}{c_n n + c_p n_i / \chi} + 1\right]^{-1} \qquad (7)$$

$$\chi = e^{\left(\frac{E - E_i}{k_B T}\right)} \qquad (8)$$

where $c_{n;p} = v_{th,e}\sigma_{e;h}$ are the capture coefficients for the electrons and holes, E the energy level, $n_i$ and $E_i$ are the intrinsic carrier density and energy, and *n; p* are the actual electron and hole densities.

The free-carrier concentrations needed for the calculation of *P* were estimated from the current measurements. To keep the calculations simple, no spatial dependence of the free-carrier concentration was taken into account. In the case of a reverse bias, the source of the current is the generation current in the depleted region, so electrons and holes contribute equally to the current. These assumptions were also kept for the current under the forward bias since details of the carrier injection from the heavily doped regions into the bulk were not known. Therefore the concentration of free electrons *n* and free holes *p* was estimated as

$$n = \frac{I}{2Av_e} \qquad p = \frac{I}{2Av_h} \qquad (9),$$

where *I* is the current, A=0,25 cm$^2$ is the surface of the diode and $v_e$ and $v_h$ are the electron and hole drift velocities estimated as $v_{e;h} = \mu_{e;h} * V/D$, where $\mu_{e;h}$ is electron (hole) mobility, *V* is the bias voltage and D=300 μm the detector thickness. The parameterization of the mobility dependence on the electric field was taken from [37]. No dependence of the mobility values on the irradiation fluence was taken into account since the effect is small for the fluences considered in this work [38]. In the case of DC light illumination the additional free-carrier density was estimated from a measurement of current increase caused by the DC light using similar relations to those in Eq. (9), and taking into account the surface of the illuminated area and the side of the illumination (e.g., if *n+* was illuminated the current increase was due to holes). It is important to note that the free-carrier concentrations (*n* or *p*)

are much lower than $N_{eff}$, so they do not influence the electric field in the diode directly. The calculations were performed with the trap parameters from Table 2.

Table II. Parameters of the defects used for the CCE calculation

| | $(E_v + E_t)$ (eV) | $g_t$ (cm$^{-1}$) | $\sigma_e$ (cm$^2$) | $\sigma_h$ (cm$^2$) |
|---|---|---|---|---|
| Acceptor | 0.57 | 1 | $15 \times 10^{-15}$ | $2 \times 10^{-15}$ |
| Donor | 0.52 | 0.07 | $1 \times 10^{-15}$ | $300 \times 10^{-15}$ |

They were chosen to be within the limits of the parameters of effective dominant electron and hole traps published in Ref. [36] and to give reasonable agreement between the calculations and the measured data. The aim of the calculations described here is to give a rough description of the various modes of operation over a wide range of fluencies using only two dominant deep traps. The simplifications made in various assumptions do not allow us to narrow the wide ranges of the parameter values from [36]. In Fig. 11 the measured and calculated CCEs are shown as a function of fluence for the reverse and forward bias at $-30^0$C.

(a)



(b)



(c)
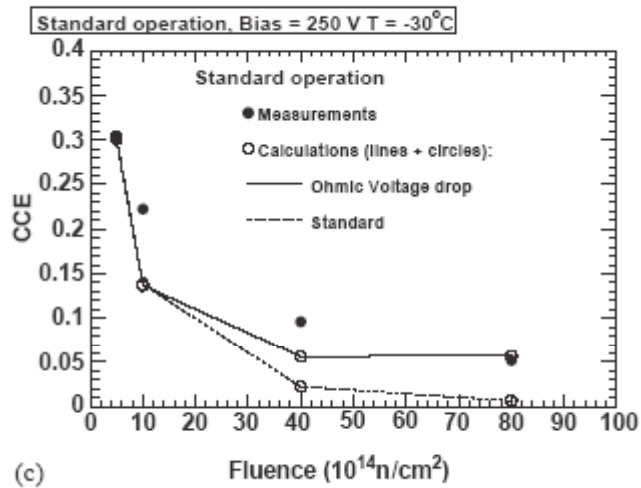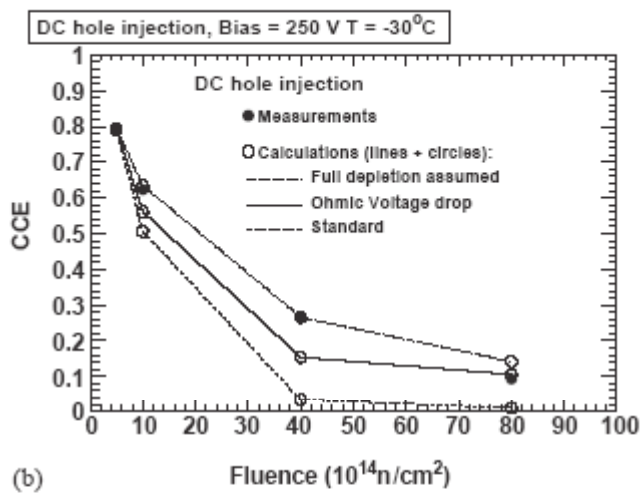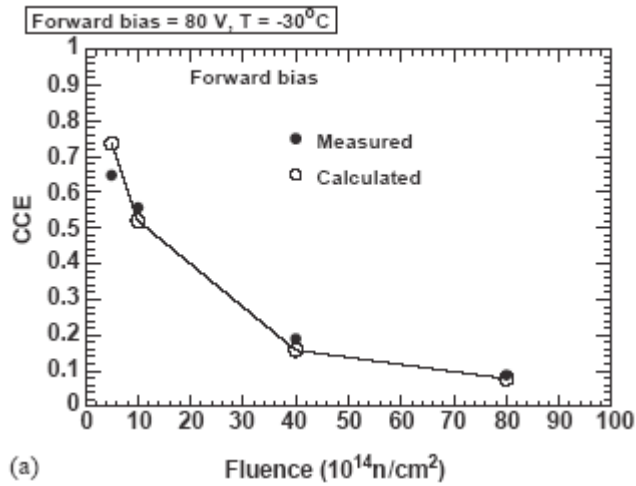
Fig. 11. Measured and calculated CCE versus fluence for (a) forward bias, (b) reverse bias with DC hole injection and (c) standard operation, all at $-30^0$C. In (b) three calculations are shown: (1) assuming a uniform field for all fluencies, considering only charge trapping, (2) calculating the depletion depth and taking into account also the voltage drop due to the resistance of the undepleted region (Ohmic Voltage Drop) and (3) ''standard calculation'' with electric field in the depleted region only. In (c) the CCE calculations with ohmic voltage drop and ''standard calculation'' are shown. Note the different scale in (c).

For the forward bias operation (Fig. 11(a)) the CCE was calculated assuming a uniform electric field $E=V/D$ throughout the whole detector thickness and taking into account only the charge trapping. A similar calculation, with a uniform electric field in the whole detector, was also made for the DC hole injection. One can see that these calculations give good agreement with the measured results. This indicates the presence of the electric field in the whole detector volume, which is a consequence of the hole injection with DC light. In the standard mode of operation the depletion depth $w$ was calculated from $w^2=2\varepsilon\varepsilon_0V/(e|N_{eff}|)$. A linear electric field in the depleted region was assumed.

The agreement with the measured data is reasonable only at the lowest fluence (see Fig. 11(c) dashed line), while the calculated values at higher fluencies are too low. Similarly, if the depletion depth and the linear field are calculated in the DC hole-injection mode, taking into account the influence of the free-hole concentration on $N_{eff}$ and trapping times given in Eq. (5)–(9), good agreement is obtained at low fluence (see Fig. 11(b), dashed line), whereas at high fluencies predicted values are much too low. The agreement between the measured and calculated results can be improved by taking into account a simple consideration: from the measurements in the forward bias mode it can be estimated that the resistivity of the detector material at higher fluencies is very high. In Fig. 12 the resistance ($R=V/I$) is plotted versus inverse of detector current $1/I$.
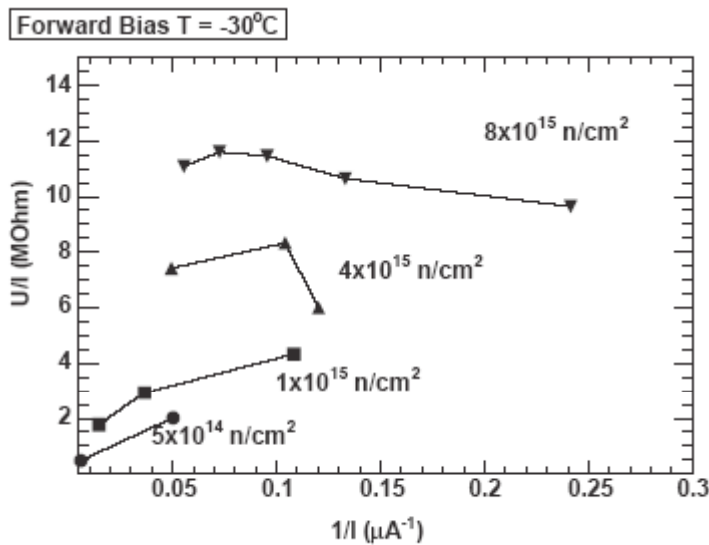


Fig. 12. Resistance $V/I$ versus inverse of current $1/I$ measured in forward bias mode at $-30^0$C.

At lower fluencies the resistance is linearly increasing with falling current, as expected for PIN diodes under forward bias [39], whereas at higher fluencies the resistance does not depend on the current and is very high. Because of such high values and the ohmic behavior of the resistance one cannot neglect the ohmic voltage drop in undepleted bulk also when operating under a reverse bias. To take this effect into account, the electric field in the CCE calculations in reverse bias mode was modified. The bias voltage was distributed between the voltage drop on the pn-junction and the ohmic voltage drop: $V_{bias}=V_{junction}+IR$, where $R$ is the resistance. The resistances for the four diodes were estimated from Fig. 12: 1, 2, 7 and 11M$\Omega$ in order of increasing irradiation fluencies. In Fig. 13 the ohmic voltage drop ($IR$) and the

voltage drop in the pn-junction ($V_{junction}$) for the DC hole-injection mode and the standard operation mode are shown as a function of fluence.
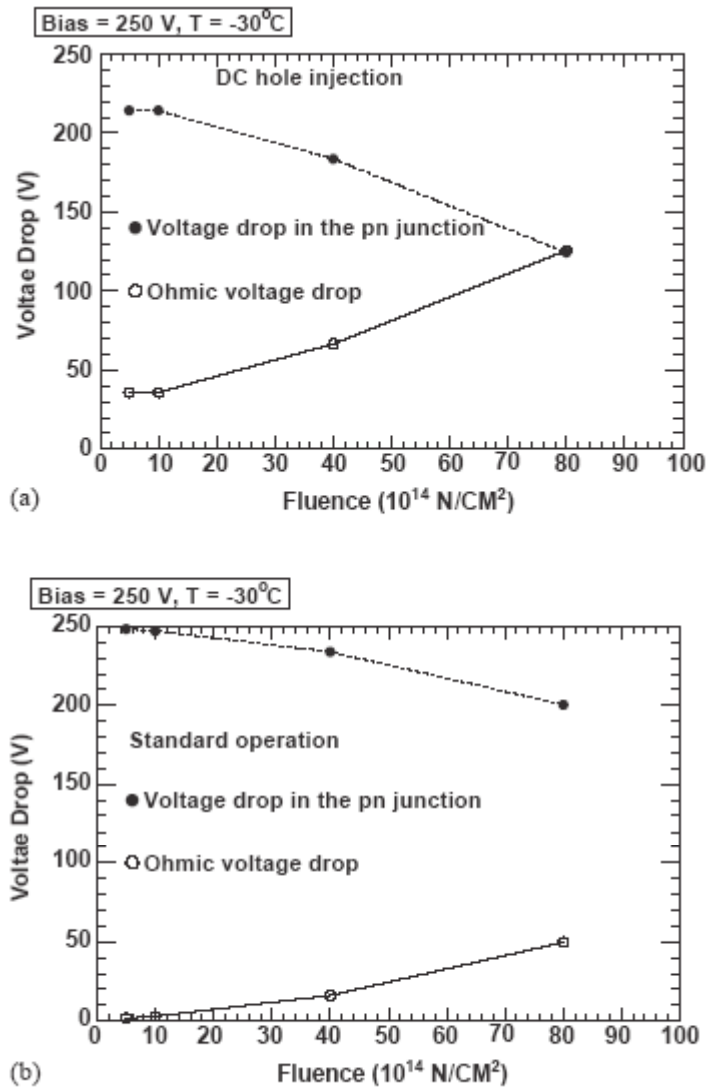


Fig. 13. Ohmic voltage drop (IR) and voltage drop in the junction (Vjunction ¼ Vbias _ IR) as a function of fluence for (a) DC hole-injection mode and (b) standard operation.

It is clear that the effect of the ohmic voltage drop for diodes irradiated with lower fluencies ($5*10^{14}$ and $1*10^{15}$ n/cm$^2$) is so small that the uncertainty of the estimated resistances has a small effect. In the pn-junction of width $w$ the electric field due to the space charge is given by

$$E_{junction}(x) = \frac{e_0 \, | \, N_{eff} \, |}{\varepsilon \varepsilon_0}(w - x) \qquad (10)$$

and the electric field due to the ohmic resistivity is $E_{ohm} = \rho j$, where $j$ is the current density, and $\rho = AR/D$ with $A$=0,25 cm$^2$ being the diodes area and $D$=0,03 cm the diode thickness. Therefore, the total electric field is $E=E_{junction} + E_{ohm}$ in the pn-junction and

$E=E_{ohm}$ elsewhere. One can see in Fig. 11 that the discrepancy between the measurements and the calculations at high fluencies is smaller if the CCE is calculated also taking into account the electric field due to the ohmic voltage drop compared to the ''standard'' calculation with electric field in the pn-junction (i.e., the depleted region) only. In Fig. 14 the measured and calculated dependence of the CCE on the bias voltage at $T=-30^0C$ is shown.
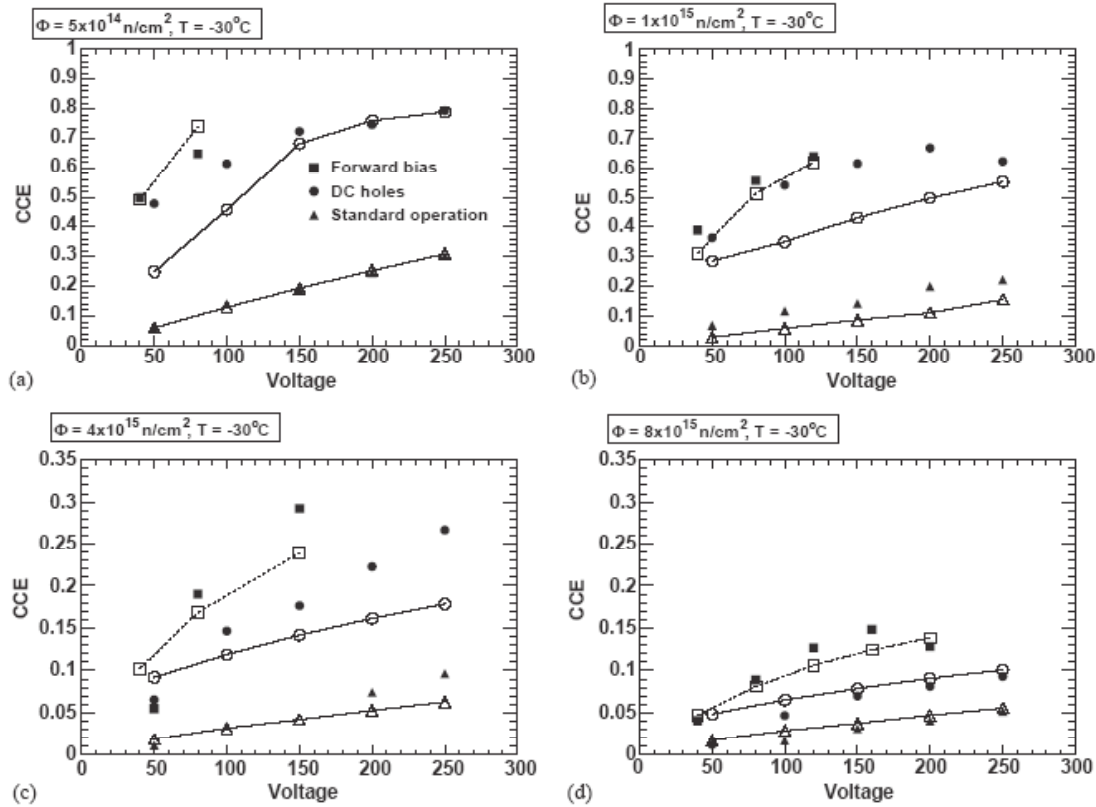


Fig. 14. Measured (full symbols) and calculated (empty symbols) CCE dependence on bias voltage for diode irradiated to various fluencies operated in standard mode, under continuous hole injection and under forward bias. Please note that the scale is not the same in all plots.

Calculations of the CCE in the DC hole-injection mode and in the standard operation were made taking into account the field due to the ohmic voltage drop. In the forward bias a uniform electric field across the whole detector thickness was assumed. Keeping in mind that several rather significant simplifications were made in the modeling, the agreement with the measured results looks quite reasonable.

## 4.  LOW TEMPERATURE OPERATION OF AVALANCHE PHOTO DIODES (APD)

### 4.1 Introduction

Driven by requirements for a low noise, high quantum efficiency, compact, mechanically robust photodetector capable of withstanding high doses of radiation ($10^{13}$ neutrons/cm$^2$) and

able to operate in high magnetic fields, we have been working with Hamamatsu to develop suitable avalanche photodiodes (APDs) [40].

Remarkably, despite their not having been particularly optimized for single photon counting, with their original application being to high energy physics [41], we have found that the Hamamatsu S8148 APDs, when cooled and operated in proportional mode with suitable amplification, offer remarkable performance. This is already competitive in many ways, or even better than existing photomultiplier technology. The S8148 has quite a large active area (5x5 mm$^2$), very low dark current, and provides very high quantum efficiency (approaching 90% ) over a very wide spectral range (see figure 15). In this paper we summarize some of this work, with emphasis placed on the characteristics of this APD when operated at or near liquid nitrogen temperatures.

## 4.2 Experimental Set-up

Measurements of the cooled APD were performed inside an evacuated stainless steel box, which was placed in a dewar which could contain liquid nitrogen. The APD was connected to a Canberra-2003BT preamplifier (located outside the dewar) via ~60 cm of coaxial cable.
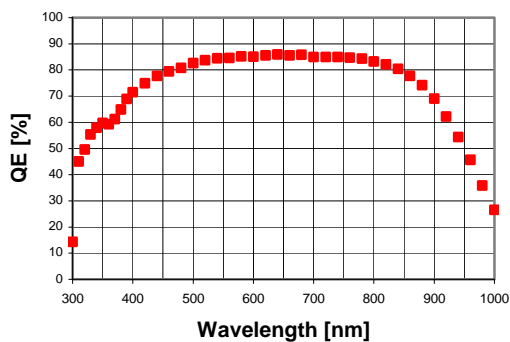


Fig. 15: Quantum efficiency as a function of wavelength

Illumination was provided by a blue (470 nm) LED through a neutral density filter. A Keithley-487 was used both as a HV-source and as a current meter. The temperature was monitored with a Pt-2000 platinum resistor.

## 4.3 Gain vs. voltage dependence

The gain of the APD as a function of voltage was measured at different temperatures using continuous illumination with the blue LED described above. Figure 16 shows the gain measured at different temperatures. A significant drop in the breakdown voltage at lower temperatures is clear for this APD.
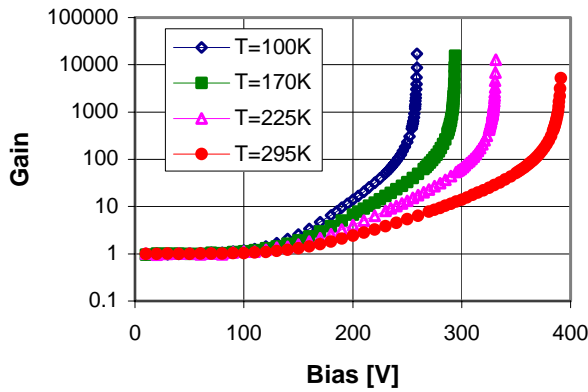
Fig. 16: Gain vs. bias measured at different temperatures

At a temperature of 100K one can see that operation at gains in excess of 10 000 is possible.

## 4.4 Dependence of the dark current on the temperature

At high gains the main source of noise is thermally generated leakage current. This thermally generated current appears, multiplied by the gain, as the bulk dark current, and dividing dark current by gain then provides a means of calculating it [42]. This ratio is plotted as a function of gain in figure 17, which shows that it is almost constant at about 12 pA at gains over 300 at room temperature.
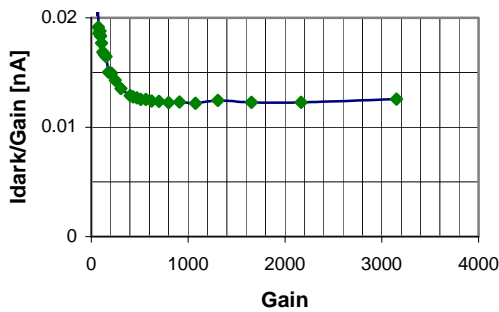


Fig. 17: Dark current divided by gain vs. gain measured at room temperature

This current corresponds to ~75 x 106 primary electrons generated thermally every second - a value, which can be significantly decreased by reducing the temperature of the APD [43].

Figure 18 shows the bulk dark current at different temperatures, with the decrease being by a factor of about 5,000 for a temperature reduction from 295 K to 222 K. It also shows a
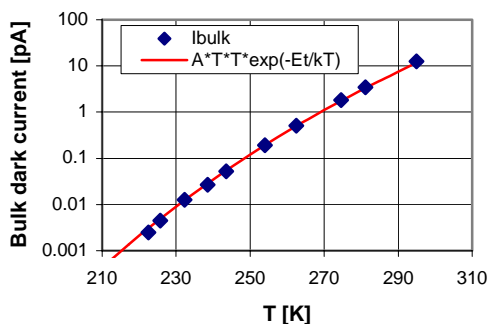
fit with the function proposed in [44], where parameter Et was found to be equal to 0.60 eV, as might be expected for silicon.

   Fig. 18: Bulk dark current dependence on temperature.

   No measurements were done below 220 K as the values of the dark current measured even at high gains became very low and we reached the sensitivity limit of our set-up. Assuming that an extrapolation based on the formula is appropriate and that there are no unexpected drops in quantum efficiency or gain, this is extremely encouraging for single photon counting with extremely low dark count rates.

### 4.5 Light and dark counting rate at T=108K using S8148 APD

   As noted earlier, Figure 16 shows that near liquid nitrogen temperatures the S8148 APD can operate at very high gain (>10 000). With the use of a low noise amplifier then, it is possible to do single photon counting. Single photon detection measurements were performed with the S8148 APD operated at a T=108K. The APD was operated at a gain of 8 000 and illuminated at constant intensity with a 470 nm LED via a neutral density filter as described earlier. A light-induced photocurrent (the difference between the total current $I_{total}$ and the dark current $I_{dark}$) of 34 pA was measured at this gain. This corresponds to 4.25 fA of primary photocurrent, or about 26500 photoelectrons generated in the APD every second. The signals from the preamplifier (Canberra-2003BT) were sent to a TENELEC TC-205A shaper operated with 3 ms shaping time. An equivalent noise charge of 430 electrons (r.m.s.) was measured when the APD was operated at 108K. A discriminator (LeCroy 623B) was used to convert all pulses above a (variable) threshold to standard logic pulses, which were counted with a 250 MHz counter.
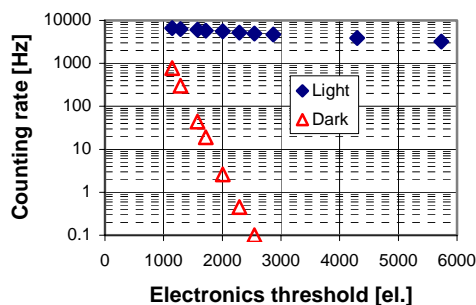


Figure 19 shows illuminated and dark counting rates versus discriminator threshold.

   Fig. 19: Light and dark counting rates as a function of electronics threshold

   A count rate of 6,6 kHz was measured when light was present at a threshold of 1150 electrons. This correspond to a detection efficiency of 25% for a single photoelectron or 20% detection efficiency for a single photon, taking into account the 80% quantum efficiency of this APD for 470 nm light.
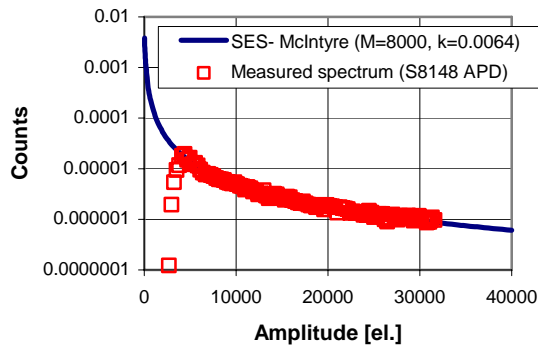
Fig. 20: APD single electron spectra (measured and calculated)

The dark count was 0,77kHz at this threshold. A very small dark count (0,1Hz) was measured at the 2550 electron threshold, while the illuminated count rate was still high (5 kHz or 19% single photoelectron detection efficiency). From Figure 19 it can be seen that the dark count rate abruptly drops with the increase of the discriminator threshold, which suggests that it is mainly due to electronics noise. The intrinsic dark count rate for operation at 108K is probably lower than 0,1 Hz.

## 4.6 Single electron spectrum

Amplitude spectra of signals from the APD were measured using a LeCroy LT342L DSO while the APD was illuminated with a low intensity light source. The DSO trigger threshold was set to 2500 electrons to avoid influence of the electronics noise on the measurement. Figure 20 shows the amplitude spectrum measured at a gain of 8000 as well as the result of a calculation of the APD single electron spectrum using the McIntyre approach [45]. The calculations were performed for an APD with a *k*-factor of 0.0064 operated at a gain of 8000. The value of the k-factor was deduced from a fit of the measurements of the excess noise factor of a S8148 APD performed in [40] with the formula:

$F=2+k*M$ (11),

where F is the APD excess noise factor and M is the APD gain (see [46]). One can see rather good agreement between measurements and calculations. Using the theoretical single electron spectrum we calculated the dependence of the expected single photoelectron detection efficiency on the electronics threshold. The result of this calculation and the results of our measurements are shown in figure 21. It is clear from this figure that higher single photoelectron efficiency can be achieved with smaller electronics threshold, at the cost of increased noise. We expect that a suitable low noise preamplifier will need to be used which can be cooled in liquid nitrogen and physically located very close to the APD.
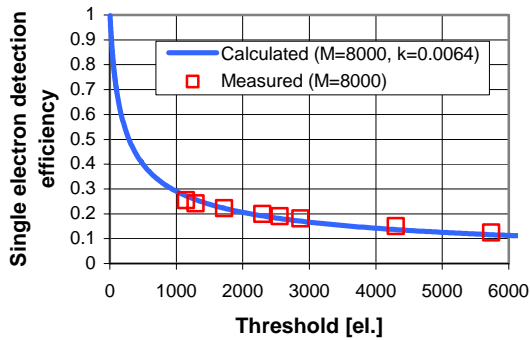
Fig. 21: Photoelectron detection efficiency, measured with S8148 APD and calculated for M=8000 and k=0.0064

## 4.7 Geiger mode operation

Very good uniformity of the avalanche process over the APD sensitive area makes possible the operation of these devices in Geiger mode. At low temperatures the dark count rate should be significantly reduced, and efficient photon counting should become possible.

For Geiger mode tests we used the same 5x5 mm$^2$ Hamamatsu APD and the same set-up as described earlier, but with the low noise preamplifier replaced with a simple passive quenching circuit.
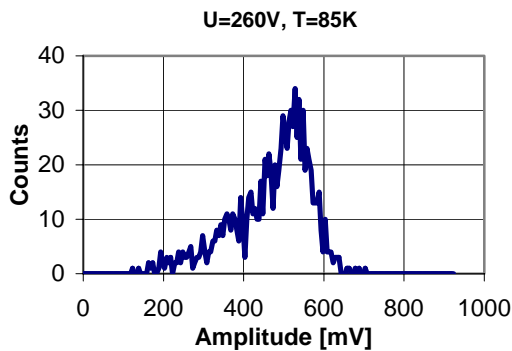


Fig. 22: Amplitude spectrum of signals from APD operated in a Geiger mode.

The amplitude distribution of one-electron signals measured with the APD operated in Geiger mode is shown in Fig. 22. The very small dispersion of one-electron signals is a result of the very good uniformity of the avalanche multiplication over the APD sensitive area. APD was illuminated with low intensity blue LED continuous light. The temperature during these tests was stabilized at 85 K and the bias voltage was 260 V (~2.5 V over APD breakdown voltage). Signals from APD were recorded at 50 Ω input of a LeCroy LT342L DSO without additional amplification. The trigger threshold was set to ~70 mV. Fig.23: Light, dark and light-dark counting rates vs. APD bias voltage (dead time corrected).
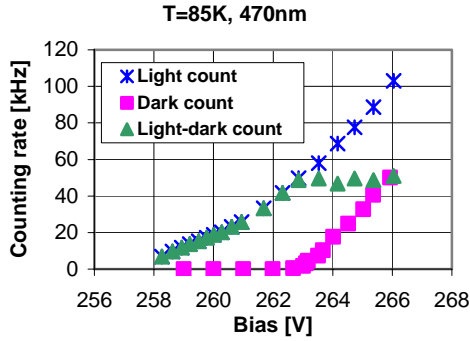
**T=85K, 470nm**

Fig. 23 shows the dependence of the APD counting rate on the bias voltage, with and without illumination.

During this measurement the APD was illuminated with 470 nm LED continuous light. A light-induced photocurrent of 70 pA was measured while the APD was operating in linear mode (below breakdown) at gain of 8000. This corresponds to 8.7 fA of primary photocurrent, or about 54300 photoelectrons generated in the APD every second.

Signals from APD were converted to logic pulses using a threshold discriminator (~50mV threshold level) and then counted by a 250 MHz counter. After each pulse, the voltage on the APD drops to its breakdown voltage and then exponentially recovers with a time constant, which is determined mainly by the APD capacitance and the value of load resistance. Fig. 24: Photon detection efficiency and dark counting rate vs. bias voltage

Taking into account this effect, light and dark counts should be corrected using the non paralyzable dead time model described in reference [47]. The dead time (t) of our counting system was measured using the "two-source method" [47] and was found to be ~4.5 ms. Corrected (true) counting rates were calculated from the measured rates using the equation:

$$Ncorr = Nmeas/(1 - Nmeas * \tau) \quad (12)$$

Corrected light, dark counting rates and their residuals are shown in Fig. 23. One can see that dependence of light-dark count rate reaches plateau at U=263V. At plateau this count rate equals 49,5 kHz, which constitutes ~91% of all photoelectrons (54300) generated in the APD every second. Taking into account quantum efficiency of APD at 470 nm (QE=80%) one can calculate that at plateau photon detection efficiency equals ~72% (see Fig. 24).
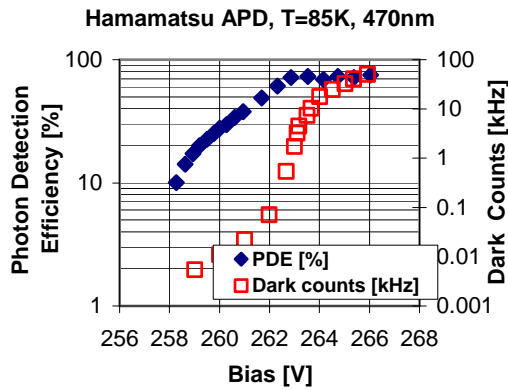
**Hamamatsu APD, T=85K, 470nm**



Fig. 24: Photon detection efficiency and dark counting rate vs. bias voltage

From Fig. 24 one can also notice very sharp increase of dark counting rate starting from U=262 V. This increase is probably because of two effects: field-assisted enhancement of emission rate from generation centers and an increase of the avalanche triggering probability [48].

Gain as a function of voltage for the Hamamatsu S8148 APD was studied over a wide temperature range: 100K-295K. At T~100K the S8148 APD operated at mean gains as high as 10 000. This APD has very small bulk dark current even at room temperature (12 pA) and decreased by a factor of ~5000, when the temperature was lowered from 295K to 222K. At 108K, 25% single photoelectron detection efficiency (or 20% photon detection efficiency) was measured with a S8148 APD operating at a gain of 8,000 and 1,150 electrons electronics threshold. An extremely low dark count rate (~0,1 Hz) was measured with a threshold of 2550 electrons, while photoelectron detection efficiency remained high (19%). Clearly there is work still to be done, but there appear to be no major obstacles to achieving photon counting with very high quantum efficiencies over a wide spectral range, and with extremely low noise.

At 85K a photon detection efficiency of 72% at 470 nm was achieved. To the best of our knowledge this is the first time that such high detection efficiency has been reported for a large area APD. The noise, however, is higher than in linear mode and the reasons for this are still under study.

## 5.   CRYOGENIC AND EDGELESS MODULE PROJECT

According to the recommendation of LHCC, RD39 continued in 2004 Cryogenic silicon detector modules project. We have studied the operation efficiency of the silicon micro-strip detectors at low-temperature [90-130] K as tracking sensors for several purposes, as imaging applications or particle detection very close to an incoming beam.

### 5.1 Study of edgeless Si-microstrip sensors

For edgeless detector studies, single sided ministrip detectors were used. The design of these detectors is similar to the ones from the tracker of the CMS experiment, i.e. p+ implants on n-type silicon substrate. The mini-sensors, which come from 320 µm thick wafers, have 196 strips, each 1.56 cm long and with a 120 µm pitch. The substrate doping concentration is between [1.40-1.85] x$10^{13}$ (cm$^{-3}$), corresponding to a full depletion bias voltage $V_{fd}$ between [100-125] V. At room temperature, the baby-sensors featured around 10 nA leakage current when operated in the constant region of the IV characteristic. They were divided in several groups in order to be cut with different geometries at Brookhaven National Laboratory, USA:

- A number of baby-detectors were cut straight, along the strips, through the p+ implant;
- Few baby detectors were cut with a small angle between strips and the cut direction;
- One baby detector was cut perpendicular to the strips direction.

We finally sorted the sensors in two sets, the 'old' sensors cut in 2003, and the 'new' sensors cut in 2004 that underwent a chemical etching procedure after laser cut.

The electrical tests were performed in a controlled environment in Louvain-clean room and the set-up consisted in a KarlSuss Probe Station, Keithley 2410 sourcemeter, Keithley 6514 electrometer for the current measurements. For all tests, dry air was flushed inside the Probe Station, in order to keep the relative humidity lower than 5%.

The detectors for each geometry were measured at several temperatures, in the range [+20; –30]°C (the lower value is the intrinsic set-up limit) to verify the dependence of the leakage current with the temperature. These measurements were repeated several times, at few months period, to study the evolution in time of the surface component of the leakage current due to the silicon crystal damage by the laser cut. The results are showing a general trend of a current increase after the laser cut which in several cases can be up to 104 times. For some cut sensors, the temperature dependence of the leakage current is very weak, and there is no apparent improvement using the etching procedure after cut. Fig.25 shows an example of a good 'candidate' for an edgeless detector module, in view of the fact that the current drops significantly with the temperature.
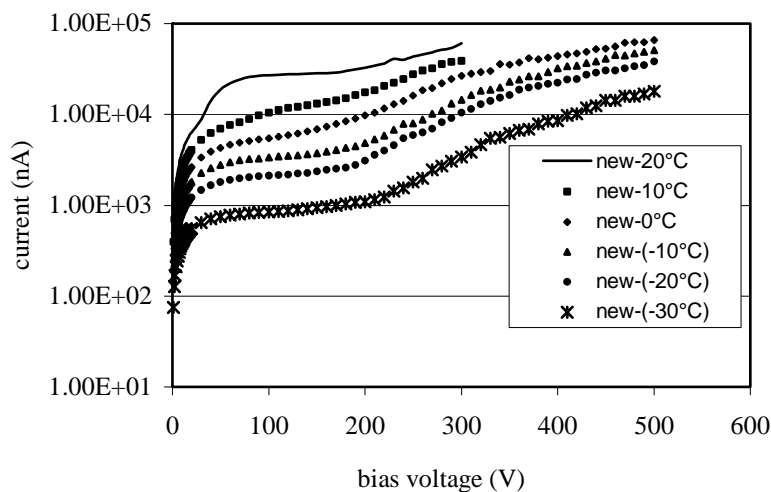


Figure 25. Temperature dependence of the leakage current of "cut along strips geometry" (July 2004, with wet etching).

For this sensor, the current increased in a period of a few months by a factor of 5 (comparison made at –30°C). This effect thus requires, once more, the operation of these detectors at a very low temperature. The time evolution of the leakage current for cut detectors without etching treatment is presented in Fig.26 and Fig 27, for half-sensors (A and B) that initially belonged to the same detector. As it can be seen, the evolution in time of the leakage current is different, which suggests that the storage conditions might be a crucial factor.
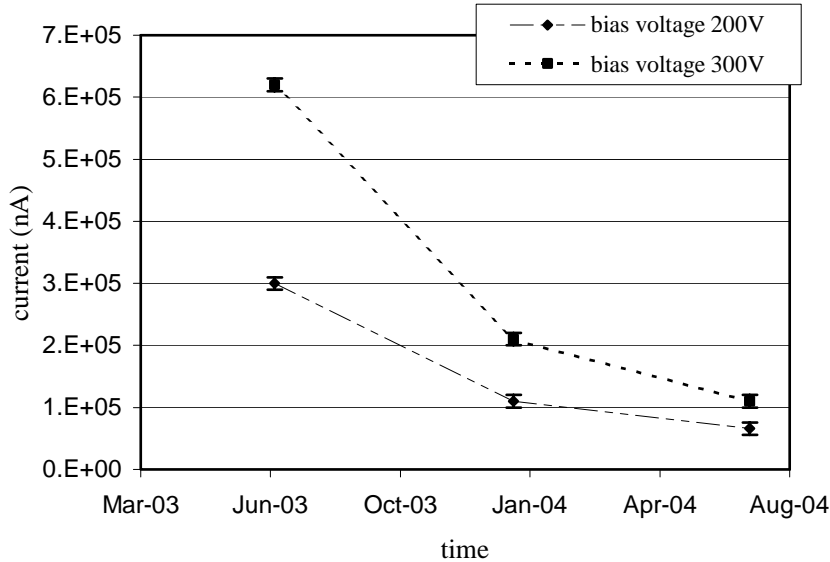
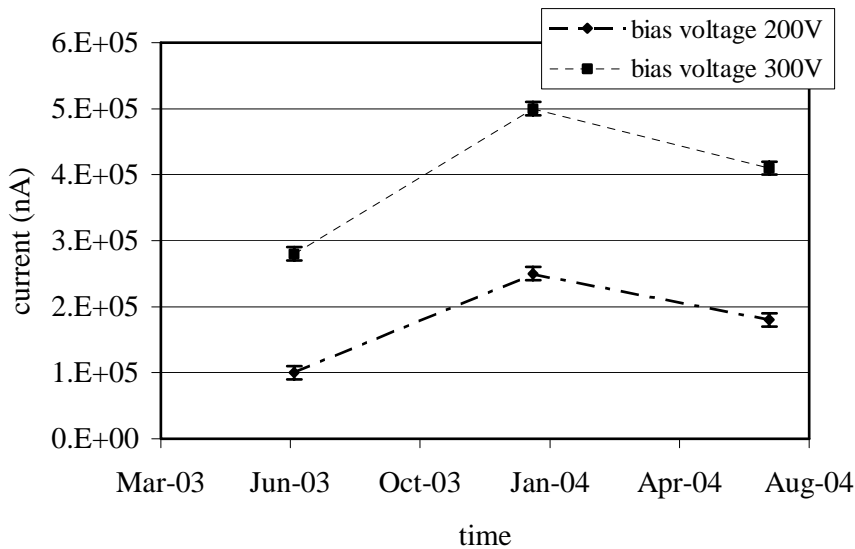Figure 26. Time evolution of the leakage current for Straight-cut A detector.

Figure 27. Time evolution of the leakage current for Straight-cut B detector.

In case of sensors with angle-cut and perpendicular-cut geometries, the temperature dependence of leakage current is peculiar. The time increase of the leakage current of these sensors imposes the necessity to discard them, for the moment, as good candidates for the cold edgeless module.

For the next future, we plan to produce several sets of baby-cut sensors from CMS production (Hamamatsu technology) and from Helsinki Institute of Physics, to compare the laser cut effects on different silicon substrates (doping concentration, impurities and geometry) and crystal growing methods.

We will assemble an 'edgeless' module in the next period from the good 'candidates', taking into consideration the leakage current behavior with temperature and in time. The goal is to determine which is the particle detection efficiency of the border micro-strips, which is significantly influenced by the silicon crystal cut. We will use two pairs of cut-along-strips geometry, with the cuts facing each other, and connected to the CMS-type readout electronics. Tests will be performed together with several reference silicon micro-strip module planes, in particle beam or with a source, to establish the track reconstruction performance in the cut region.

This module is planed to operate at very low temperature 90-130 K, to keep the leakage current as low as possible, therefore the cooling system and the readout electronics (see 5.3 of this chapter) are a decisive part of the edgeless module performance.

## 5.2 Characterization of CMS tracker hybrids at low temperatures

The read-out electronics of the cryogenic and the edgeless modules have been chosen to be the CMS tracker hybrids, which include the APV25 [49] read-out chips. The operation of APV25 in cold temperature has already been proved [50], but as the structure of the hybrid itself is more complex, its ability to work at low temperatures has to be verified.

The CMS tracker hybrid consists in a frame, in ceramics in early designs and now in kapton on ceramics, with several chips for the data acquisition and basic processing, and for synchronization and control. The APV25s [49] are non-encapsulated acquisition chips, with 128 input channels, a signal shaper and preamplifier, a pipeline and an internal multiplexer, which outputs analog data. In order to match the LHC collision rate, at low or high luminosity, the APV25 chip can be operated in two modes, peak or deconvolution. Depending on its type, either 4 or 6 APVs are mounted on a hybrid. The PLL chip [51] handles the clock and trigger signals. The output signals from all the APV25s are gathered by the MUX chip [52] on fewer  differential data lines. The currents and voltages were controlled by using a 12bit ADC, the DCU chip [53]. A unique NAIS connector, at the end of a small kapton cable, allows the connection to the power supplies and the data and control signals.

The CMS tracker hybrid has been designed to be operated down to about –20°C. Using two dedicated test setups, operation of hybrids at lower temperatures have been investigated. The setup is based on a chuck cooled with liquid nitrogen and heated with resistors. A pt100 probe helps an external controller to set the chuck temperature. The newest setup is equipped with a dry air inlet, as well as a sensor for relative humidity and ambiance temperature, preventing from potential problems of a wet atmosphere. A good contact with the chuck, ensured by a vacuum line, cools the hybrid to the target temperature. Finally, a high voltage connection has also been foreseen for later tests of cryogenic modules. The test setup is shown in Fig. 28.
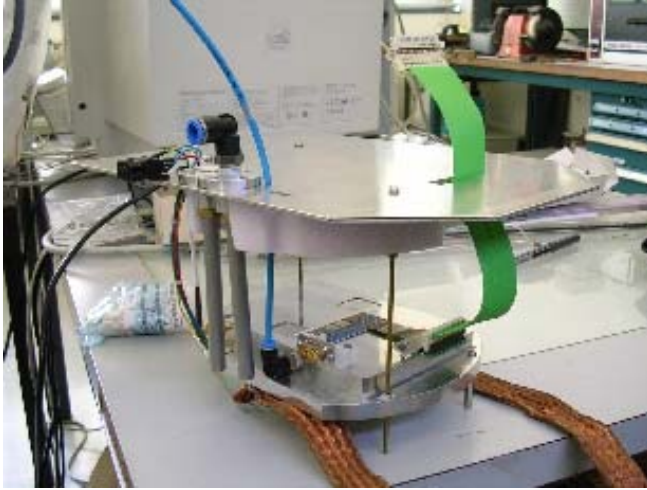
Fig. 28. Setup for characterization of CMS tracker hybrids at low temperatures.

The official CMS test software [54] and acquisition system have been used for the characterization of the hybrids in the cold. However, a software patch was needed for the dedicated initialization of the PLL at low temperatures. The operation of hybrids was possible down to 207K, but this limit temperature fluctuates with the tested hybrid. The results of these low temperature tests deal with the pedestal, the noise and common mode, the pulse shape and the gain data (fig.29).
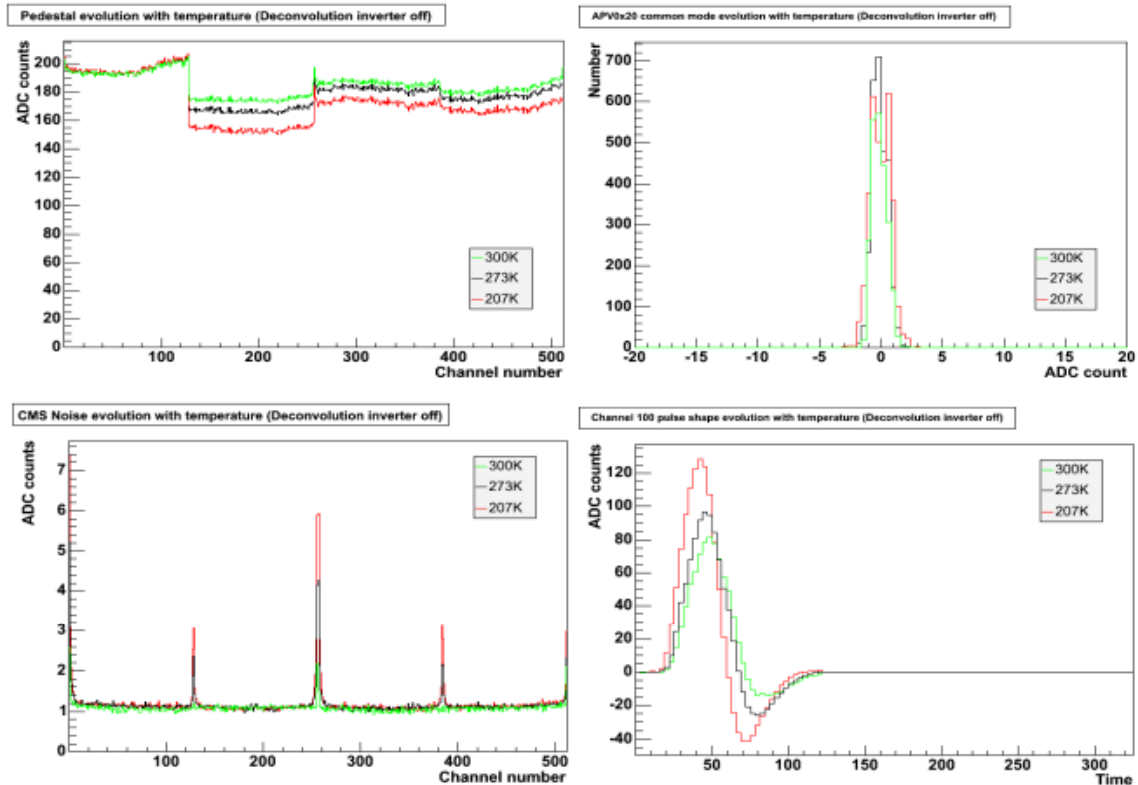


Fig.29: Pedestal, Common mode, Common mode-subtracted noise and Pulse shape evolution with temperature for a CMS tracker hybrid.

As naively expected, the pedestal of the data is slightly decreasing, which could be interpreted in lower thermal noise at the input stages of the APV25 channels. However, the evolution of the pedestal data on a single hybrid depends from chip to chip and on the operating modes of the chip. Amongst the common mode, the raw noise and the common-mode-subtracted noise, none significantly changes. Only noises for the channels corresponding to the APV edges seem to increase. This behaviour is interpreted as computational artifacts, but has still to be further investigated. Pulse shapes show higher amplitude and shorter rise time. Such behaviour has also been reported by the CMS collaboration [55], for a complete module.

### 5.3 Module assembly and test

We built our first cryogenic full-size module, from a 380 mm thick float-zone silicon sensor with 1024 strips, 50 mm pitch, 6 cm strip length, delivered by Helsinki Institute of Physics. The silicon sensor is laying on a silicon support plate provided with a metallic deposition in contact, through the conductive glue, to the detector's backplane. The pitch adapter, which makes the necessary transition between the sensors strips to the readout channels, is done on a silicon substrate, as well. Under the pitch adapter is the carbon fibre spacer with cooling micro tubes with 0.5 and 0.6 mm, inner and outer diameter, respectively. The readout electronics consists on a ceramic CMS-type hybrid with 6 APV25 acquisition chips. The detector bias is facilitated by the wire-bondings between the silicon support metallization and the RC filter, laterally glued to the module (see [56] for more details about module assembly).

Several tests will be performed on this module in the future, concerning mostly on the strip signal reading ability and the charge collection efficiency dependence on the temperature.
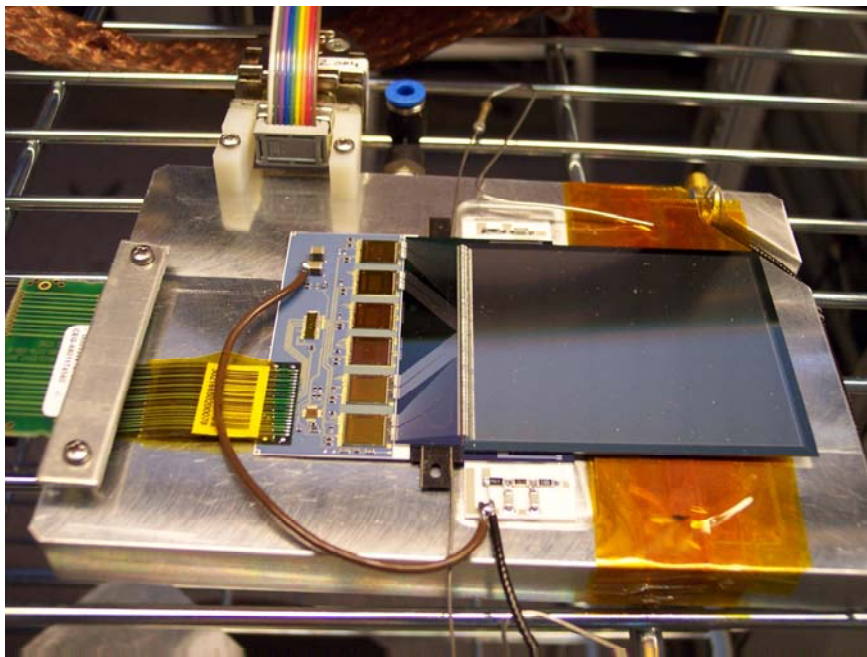


Fig. 30. Silicon strip detector attached in a cryogenic module.

# REFERENCES

[1]   G. Lindstrom & al, Nucl. Instr. and Meth. **A426** (1999) 87.
[2]   J. Härkönen et al., Nucl. Instr. And Meth. **A514** (2003) 173.
[3]   Z.Li et al., IEEE Trans. Nucl. Sci. **39** (6) (1992) 1736.
[4]   E. Tuominen et al., IEEE Trans. Nucl. Sci **50** (2003) 1942.
[5]   Z.Li et al., submitted to IEEE Trans. Nucl. Sci.
[6]   B. Dezillie, V. Eremin, Z. Li and E. Verbitskaya, Nucl. Instr. and Meth. **A452** (2000) 440.
[7]   F. Gianotti et al. hep-ph/0204087: April 2002.
[8]   E. Verbitskaya et al, Nucl. Instr. and Meth. **A 514** (2000) 47.
[9]   V. Eremin, Z. Li and E. Verbitskaya, Nucl. Instr. and Meth. **A476** (2002) 556.
[10] Z. Li et al., Nucl. Instr. and Meth. **A388** (1997) 297.
[11] M. Moll, PhD thesis, Univ. of Hamburg, (1999).
[12] E. Fretwurst et al., Nucl. Instr. and Meth. **A388** (1997) 356.
[13] E. Tuovinen et al., "Czochralski Silicon Detectors irradiated with high and low energy protons", 4th RD50 Workshop. CERN.
[14] G. Kramberger et al, Nucl. Instr. and Meth. **A481** (2002) 297.
[15] RD39 Status Report, CERN-LHCC-2003-060 (2003).
[16] V. Eremin, Z. Li, I. Ilyashenko, Nucl. Instrum. Meth., **A355**, p. 458, (1995).
[17] E. Verbitskaya, et al.,IEEE Trans. Nucl. Sci. **49**, no. 1, pp. 258 –263, 2002.
[18] L.J.Beattie, A. Chilingarov, T. Sloan, Nucl. Instr. and Meth. **A439** pp. 293-302, 2000.
[19] M. Lampert, P. Mark, "Current injection in solids", Academic Press, NY, London, 1970.
[20] Z. Li, C. J. Li, V. Eremin, E. Verbitskaya, Nucl. Instr. Meth., pp. 297-307, 1997.
[21] V. Eremin, E. Verbitskaya, Z. Li, Nucl. Instr. and Meth. **A476**, pp. 537-549, 2002.
[22] V. Eremin, Z. Li, I. Iljashenko, Nucl. Instr. and Meth. **A360** (1995) 458.
[23] G. Kramberger, et al., Nucl. Instr. and Meth. **A497** (2003) 440.
[24] G. Lutz, Nucl. Instr. and Meth. **A377** (1996) 234.
[25] A. Chilingarov, T. Sloan, Nucl. Instr. and Meth. **A399** (1997) 35.
[26] L.J. Beattie, A. Chilingarov, T. Sloan, Nucl. Instr. And Meth. **A439** (2000) 293.
[27] M. Zavrtanik, et al., IEEE Trans. Nucl. Sci. NS-49 (1)(2002) 264.
[28] V. Cindro, et al., Nucl. Instr. and Meth. **A518** (2004) 343.
[29] K. Borer, et al., Nucl. Instr. and Meth. **A440** (2000) 5.
[30] L. Casagrande, et al., Nucl. Instr. and Meth. **A477** (2002) 299.
[31] E.S. Krigtof, Avon Books, New York, September 7–10, 1998, p. 43.
[32] M. Ravnik, R. Jeraj, Nucl. Sci. Eng. 145 (2003) 145.
[33] E. Verbitskaya, et al., Nucl Instr. and Meth. **A514** (2003).
[34] S. Ramo, Proc. IRE 27 (1939) 584.
[35] G. Kramberger, et al., Nucl. Instr. and Meth. **A457** (2001) 550.
[36] G. Kramberger, et al., Nucl. Instr. and Meth. **A516** (2004) 109.
[37] D.M. Caughey, R.E. Thomas, Proc. IEEE 52 (1967) 2192.
[38] T.J. Brodbeck, et al., Nucl. Instr. and Meth. A 477 (2002) 287.
[39] S.M. Sze, Physics of Semiconductor Devices, Wiley, New York, 1981.
[40] Dieters, K. et al., 2001, Nucl. Instr. and Meth., A461 ,574.
[41] CMS ECAL Technical Design Report, November 1997, CERN/LHCC 97-33,
[42] Karar A., et al., 1999, Nucl. Instr. and Meth., A428, 413.
[43] Sze,S. M., 1985, Semiconductor devices, John Wiley and Sons.
[44] Borchi, E. and Bruzzi, M.,1994, Radiation damage in silicon detectors, Riv. del N. Cim. 17, No.11.
[45] McIntyre, R. J., 1972, IEEE Trans. Electron Devices, ED-19, 703.
[46] McIntyre, R. J., 1966, IEEE Trans. Electron Devices, ED-13,164.
[47] Knoll, G.F., 2000, Radiation detection and measurement, John Wiley and Sons.
[48] Cova, S. et al., 1996, Appl. Opt., 35, 1956.
[49] Turchetta et al., Nucl. Instr. and Meth. A 466 (2001) 359.
[50] H.Angerer et al., Nucl.Instr. and Meth., A512 (2003)
[51] P. Placidi et al., CMS Tracker PLL Reference Manual, Version 2.1,2000.
[52] P. Murray, APVMUX User Guide, Version 1.0, 2000.
[53] G. Magazzu,et al., DCU2 User Guide,Version 2.12,2001.
[54] W Beaumont, Lt software, http://hep.uia.ac.be/cms/testing/
[55] Raymond, APV settings at cold temperatures, CMS tracker week, Oct 2004
[56] Blanca Perea Solano, PhD Thesis CERN, 2004, ISBN: 84-688-8952-0.